Geophysical Journal International

Geophys. J. Int. (2015) **201,** 429–443
GJI Seismology

doi: 10.1093/gji/ggv024

Directionality of ambient noise on the Juan de Fuca plate: implications for source locations of the primary and secondary microseisms

Ye Tian and Michael H. Ritzwoller

Center for Imaging the Earth's Interior, Department of Physics, University of Colorado at Boulder, Boulder, CO 80309-0390*, USA.*
E-mail: ye.tian@colorado.edu

Accepted 2015 January 13. Received 2015 January 9; in original form 2014 September 4

SUMMARY

Based on cross-correlations of ambient seismic noise computed using 61 ocean bottom seismometers (OBSs) within the Juan de Fuca (JdF) plate from the Cascadia Initiative experiment and 42 continental stations near the coast of the western United States, we investigate the locations of generation of the primary (11–20 s period) and secondary (5–10 s period) microseisms in the northern Pacific Ocean by analysing the directionality and seasonality of the microseism (Rayleigh wave) signals received in this region. We conclude that (1) the ambient noise observed across the array is much different in the primary and secondary microseism bands, both in its azimuthal content and seasonal variation. (2) The principal secondary microseism signals propagate towards the east, consistent with their generation in deep waters of the North Pacific, perhaps coincident both with the region of observed body wave excitation and the predicted wave–wave interaction region from recent studies. (3) The primary microseism, as indicated by observations of the azimuthal dependence of the fundamental mode Rayleigh wave as well as observations of precursory arrivals, derives significantly from the shallow waters of the eastern Pacific near to the JdF plate but also has a component generated at greater distance of unknown origin. (4) These observations suggest different physical mechanisms for generating the two microseisms: the secondary microseisms are likely to be generated by non-linear wave–wave interaction over the deep Pacific Ocean, while the primary microseism may couple directly into the solid earth locally in shallow waters from ocean gravity waves. (5) Above 5 s period, high quality empirical Green's functions are observed from cross-correlations between deep water OBSs and continental stations, which illustrates that microseisms propagate efficiently from either deep or shallow water source regions onto the continent and are well recorded by continental seismic stations.

Key words: Interferometry; Surface waves and free oscillations; Wave propagation.

1. INTRODUCTION

In the past decade, tomography based on ambient seismic noise cross-correlations has proven to be a reliable basis for inference of crustal and uppermost mantle structure. It has been successfully applied to many regions across the globe (e.g. Yao *et al.* 2006; Lin *et al.* 2007, 2008; Moschetti *et al.* 2007; Yang *et al.* 2007, 2010) since its first development by Shapiro *et al.* (2005) and Sabra *et al.* (2005). Compared to traditional methods, ambient noise tomography reduces dependence on earthquakes, extends analysis to shorter periods and provides higher resolution constraints on Earth's shallow structure.

The reliability of ambient noise tomography is based on the assumption that the ambient noise field becomes approximately homogeneously distributed in azimuth of propagation when averaged over sufficiently long times. In practice, however, noise sources are often heterogeneously distributed (e.g. Stehly *et al.* 2006; Yang & Ritzwoller 2008) and persistent localized noise sources exist in some places (e.g. Shapiro *et al.* 2006; Zeng & Ni 2010; Zheng *et al.* 2011; Gu & Shen 2012). Recent studies have demonstrated that noise source locations and mechanisms can affect the accuracy of tomography obtained from cross-correlations (Tsai 2009; Weaver *et al.* 2009; Yao & van der Hilst 2009; Harmon *et al.* 2010). Better knowledge of the mechanism and distribution of ambient noise is of fundamental importance to understand the generation of microseisms, but it is also important to assess the accuracy and reliability of the results from ambient noise tomography.

The generation of microseisms has been studied for over a century. Microseisms were first hypothesized by Wiechert (1904) to be generated by surf activities along coasts and studies in the first

half of the twentieth century associated them with storm activities. The dominant frequencies of microseisms, however, were observed to be roughly twice the principal ocean gravity wave frequency (the secondary microseism). This observation gave rise to the development of the double frequency wave–wave interaction theory, which was first discussed by Miche (1944) and extended by Longuet-Higgins (1950). Hasselmann (1963) extended the double frequency theory to random waves and, furthermore, developed the theoretical basis for microsiesms with frequency content similar to the ocean gravity wave (the primary microseisms). These studies, although focused on the generation of surface (Stoneley and Rayleigh) waves, consider sources that generate all seismic modes including surface and body waves (Longuet-Higgins 1950; Ardhuin *et al.* 2011). The theories governing the generation of both primary (∼11–20 s period) and secondary (∼3–10 s period) microseisms have been supported by several recent studies (e.g. Kibblewhite & Ewans 1985; Kedar *et al.* 2008). In the primary microseism band, most studies infer shallow water sources (e.g. Hasselmann 1963; Cessaro 1994; Bromirski & Duennebier 2002). This is consistent with the theoretical understanding that ocean wave energy transfers into the solid earth by direct coupling in the primary band, which only occurs in relatively shallow regions where the water depth is comparable to the wavelength of the deep water gravity wave (Hasselmann 1963). In the secondary microseism band, generation areas have been inferred in both the deep ocean and the shallow water regions in certain locations (Bromirski *et al.* 2005; Ardhuin *et al.* 2011; Kedar 2011; Hillers *et al.* 2012). Kedar *et al.* (2008) and Ardhuin *et al.* (2011) verified with numerical wave modelling that the observed secondary microseisms, dominated by surface waves (e.g. Haubrich & McCamy 1969), can be accounted for by wave–wave interaction (Longuet-Higgins 1950) both in the deep ocean with either wind waves or independent wave systems and near the coast with coastal reflected waves. It was, however, suggested by Bromirski *et al.* (2005, 2013) that deep water generated double frequency microseism energy is seldomly recorded by continental stations and land observations are dominated by near-coastal wave activity. Moreover, it is not clear whether the primary and the secondary microseisms share the same shallow water source regions (Cessaro 1994; Bromirski & Duennebier 2002) and persistent noise sources have been observed at different locations across the globe (Cessaro 1994; Zhan *et al.* 2010; Zeng & Ni 2010; Gu & Shen 2012).

Observations of the source locations based on ambient noise cross-correlations, on the other hand, are as yet quite limited. It is important, however, to make such observations because the data normalizations and the time averaging processes that occur as part of preparing data for cross-correlation tend to obscure the real source distributions and homogenize the intensities of different sources. On a global scale, Stehly *et al.* (2006) and Yang & Ritzwoller (2008) investigated the source location of ambient noise using cross-correlations of ambient noise by analysing data from continental stations located in Europe, Africa and the western and eastern United States. These studies, although based on similar data, arrived at different conclusions concerning the source locations, where Stehly *et al.* concludes that the primary microseism band is dominated by deep water sources and the secondary microseism band is mostly affected by shallow water sources, while Yang *et al.* argues for shallow water sources at all periods based largely on the principle of parsimony. On a regional scale, most studies argue for shallow water sources for both the primary and secondary microseisms (e.g. Gu *et al.* 2007; Chen *et al.* 2011; Köhler *et al.* 2011). Gu & Shen (2012), however, made a similar analysis for secondary microseisms in southwestern Canada and observed seismic energy coming from the Pacific Ocean, which is similar to observations of body waves from other microseism studies (e.g. Gerstoft *et al.* 2008; Landès *et al.* 2010). Enigmatically, they also observed a persistent localized noise source near Lesser Slave Lake. The inconsistent conclusions between these studies are at least partially caused by limitations in the observations used, particularly a lack of observations in the ocean, which could possibly be solved with a combined use of ocean bottom seismometers (OBSs) and near coastal on-land stations. The recent deployment of OBSs by the Cascadia Initiative experiment on the Juan de Fuca (JdF) plate and the open availability of these data provides such an opportunity to investigate the source locations of microseisms received in this region. The OBS data were the basis for an earlier ambient noise tomographic study of the JdF plate performed by Tian *et al.* (2013).

In this paper, we investigate ambient noise cross-correlations obtained from OBSs situated on the JdF plate as well as on-land stations located in Washington, Oregon and Northern California and address the following four questions. First, we consider here whether the primary and secondary microseisms are generated at the same locations by analysing the directionality of the cross-correlation signals observed in the study area. Secondly, we investigate whether there are ambient noise signals that are generated in deep waters of the North Pacific. Thirdly, we search for evidence of shallow water sources of ambient noise and determine whether they are continuously or discretely distributed in space. Finally, we investigate the continuity of the microseism wavefields from the oceanic to the continental parts of the study region by determining whether deep water generated signals recorded on the OBSs propagate onto the continent.

2 DATA AND MEASUREMENTS

This study is based on ocean bottom seismograph (OBS) data obtained in the first year of the Cascadia Initiative experiment along with data from EarthScope USArray stations in the western United States, as shown in Fig. 1(a). We use data from 61 OBS stations (the vertical channel of station J48A failed during the deployment) together with 42 continental stations near the west coast of the states of Washington, Oregon and northern California (11 of which are to the east of the region shown in Fig. 1a). At least 6 months of continuous data that overlap in time are available from the 61 OBSs and the 42 continental stations from late November 2011 to early May 2012.

We compute the cross-correlations between vertical component records for all stations after applying traditional ambient noise data processing including running average time-domain normalization and frequency domain normalization (Bensen *et al.* 2007), such as those shown in Figs 1(b) and (c). However, in addition, because of the large number of small earthquakes bordering the JdF plate, prior to cross-correlation we further down-weight time intervals when earthquake activity is particularly high. Fig. 1(b) shows an example cross-correlation between OBS stations J23A and J47A, which are identified in Fig. 1(a). The frequency-time analysis (FTAN) diagram of the 'symmetric component' (the average between positive and negative lags) of the cross-correlation is shown below the cross-correlation with the measured group and phase speed curves indicated, respectively, by white and blue dots. A first-overtone is also observed between periods of 2 and 5 s, but overtone signals are not used in this study. An example cross-correlation between continental stations I03D and I05D and its FTAN diagram are presented

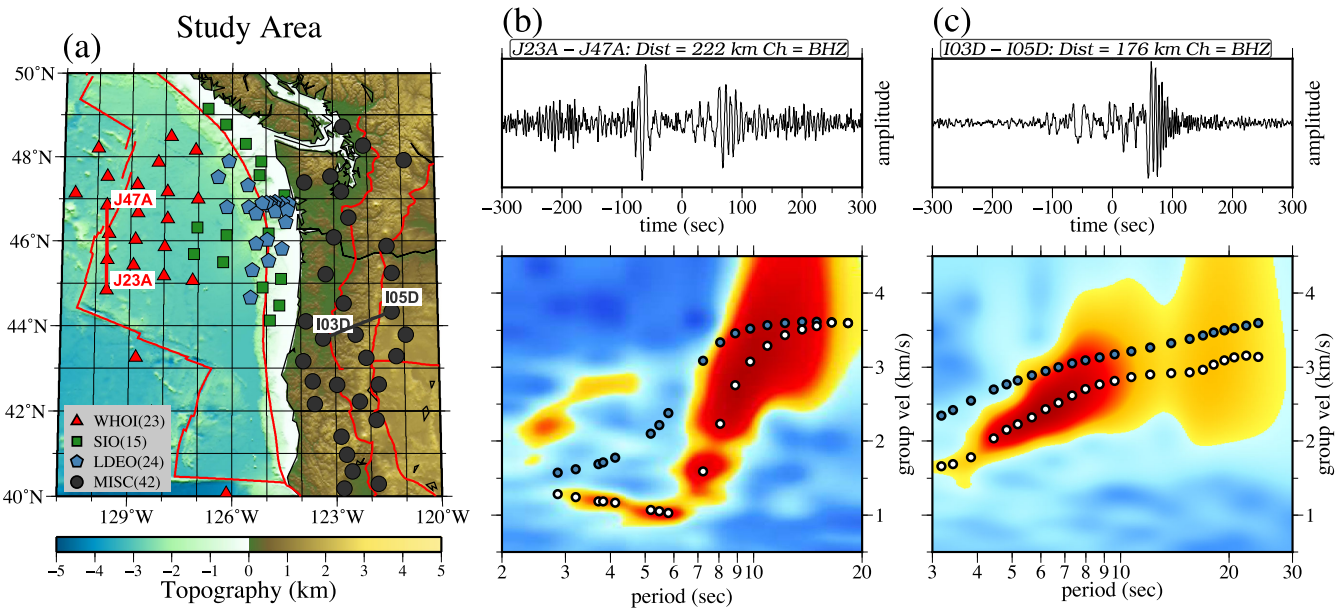

Figure 1. (a) Locations of the 62 Cascadia Initiative OBS stations are plotted over bathymetry/topography with the Juan de Fuca Ridge, the plate boundary, and continental tectonic regions shown as red lines. OBS stations from three different institutions are plotted with red triangles (WHOI), green squares (SIO) and blue pentagons (LDEO) while the continental stations are plotted with grey circles. (b) Example 6 month cross-correlation of vertical component ambient noise between stations J23A and J47A, marked as the red interstation path in Fig. 1(a), and the corresponding symmetric component group velocity versus period (FTAN) diagram. Background colour indicates the spectral amplitude and the group and phase speeds are indicated with white and blue circles, respectively. A 1st overtone signal is seen between 2 and 5 s periods with group speeds between 2 and 3 km s^{-1}. (c) Same as (b), but for continental stations I03D and I05D, marked as the grey interstation path in Fig. 1(a).

in Fig. 1(c) where the group and phase speeds vary less over period in comparison to the oceanic path.

Cross-correlations of ambient noise can be used to determine the azimuthal content of the ambient noise (e.g. Stehly *et al.* 2006; Yang & Ritzwoller 2008), based on the principle that long-duration cross-correlations are primarily sensitive to opposing waves propagating between the two stations. There are two primary caveats. (1) Time domain normalization tends to accentuate distant sources over local sources. (2) Sources that are not approximately in-line with the two stations produce precursory signals that may be persistent features of the cross-correlations even for very long time-series. Such precursory signals have been used to study persistent localized sources such as the Gulf of Guinea microseism (Shapiro *et al.* 2006) and the Kyushu microseism (Zeng & Ni 2010; Zheng *et al.* 2011). In attempting to ensure that such precursory signals do not interfere with our measurements of the directional dependence of ambient noise, in addition to 'down-weighting' the times of frequent local earthquakes in producing the cross-correlations, we update the FTAN measurements iteratively based on a set of reference group and phase speed dispersion curves. The reference dispersion curves are first generated based on a lithospheric age–speed relationship as described by Tian *et al.* (2013) and then updated after discarding paths that we identify with clear precursory signals. Also, as will be discussed later, precursory signals are observed mainly in the primary microseism band. Measurements affected by strong precursory signals typically still have reasonable surface wave dispersion in the secondary microseism band. Any erroneous measurements in the primary band produce a large jump in the dispersion curve between the two bands which are identified as bad measurements in the FTAN process (Levshin & Ritzwoller 2001).

Because absolute amplitude information is lost during the processing of ambient noise data, we measure only relative Rayleigh wave amplitude by using the signal-to-noise ratio (SNR). Fig. 2 illustrates how SNR is measured. We measure SNR in the time domain after narrow band filtering, defining it as the peak signal to the rms trailing noise separately on each lag of the cross-correlation. The two lags represent waves travelling in opposite directions between the two stations where positive lag is associated with waves propagating from the first to the second station in a named station-pair, where the first station is called the 'central station'. Our simulations indicate that a SNR > 3 implies that a Rayleigh wave signal exists above the noise level. This is established by measuring SNR on noise rather than on signal. In time windows where only noise is present, the SNR is seldom greater than 3. Other examples of the measurement of SNR in a different frequency band are presented in Fig. 3(a).

For each central station, we sort the cross-correlations into a set of outgoing waves and incoming waves. We plot the SNR for the outgoing waves at the central station and the SNR for the incoming waves at the other stations in the cross-correlations. Fig. 3(b) illustrates how the SNR of the outgoing waves can be presented in map form to display information about the azimuthal content of ambient noise. The orange arrows emanating from station J44A point to the other stations in the cross-correlations, corresponding to outgoing waves. The blue arrows assigned to the neighbouring stations point to J44A and correspond to waves coming into that station. Note that for a cross-correlation between two stations A and B, incoming waves for station A are outgoing waves for station B. Thus, all SNR measurements are used, but we assign a measurement to the location of the station for which the measurement corresponds to the outgoing wave. The results for many stations simultaneously are presented in what we call a 'fan diagram' (inset diagram on the right-hand side in Fig. 3b), in which SNR is colour-coded and plotted as same-length bars that point in the direction of wave propagation (i.e. away from the source). In producing the fan diagram, we first correct all SNR measurements for geometrical spreading

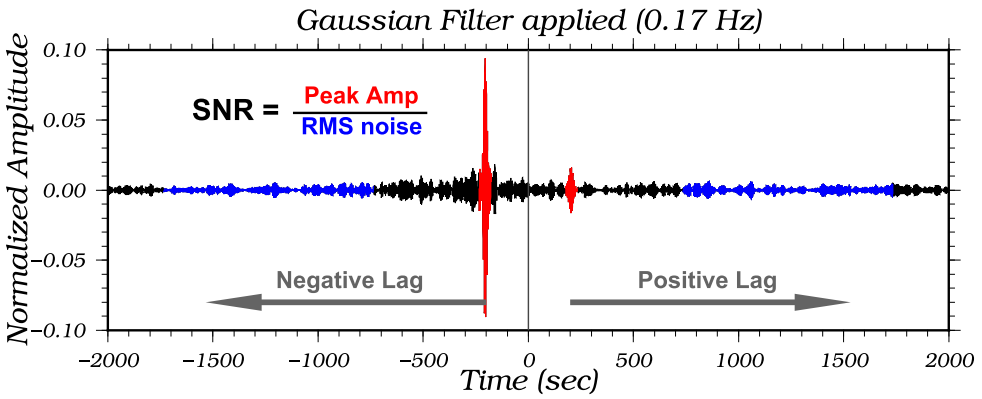

Figure 2. Illustration of the measurement of signal-to-noise ratio (SNR). The ambient noise cross-correlation between OBS stations J30A and J44A (identified in Fig. 3b) is filtered around centre frequency 0.17 Hz in the secondary microseism band. The signal windows are centred on the Rayleigh wave group time measured by frequency-time analysis (FTAN) and are marked in red. The noise windows begin 500 s after the signal, are 1000 s in duration, and are marked in blue. The SNR is defined as the peak amplitude in the signal window divided by the rms of the amplitude in the noise window, and is computed for a set of centre frequencies.

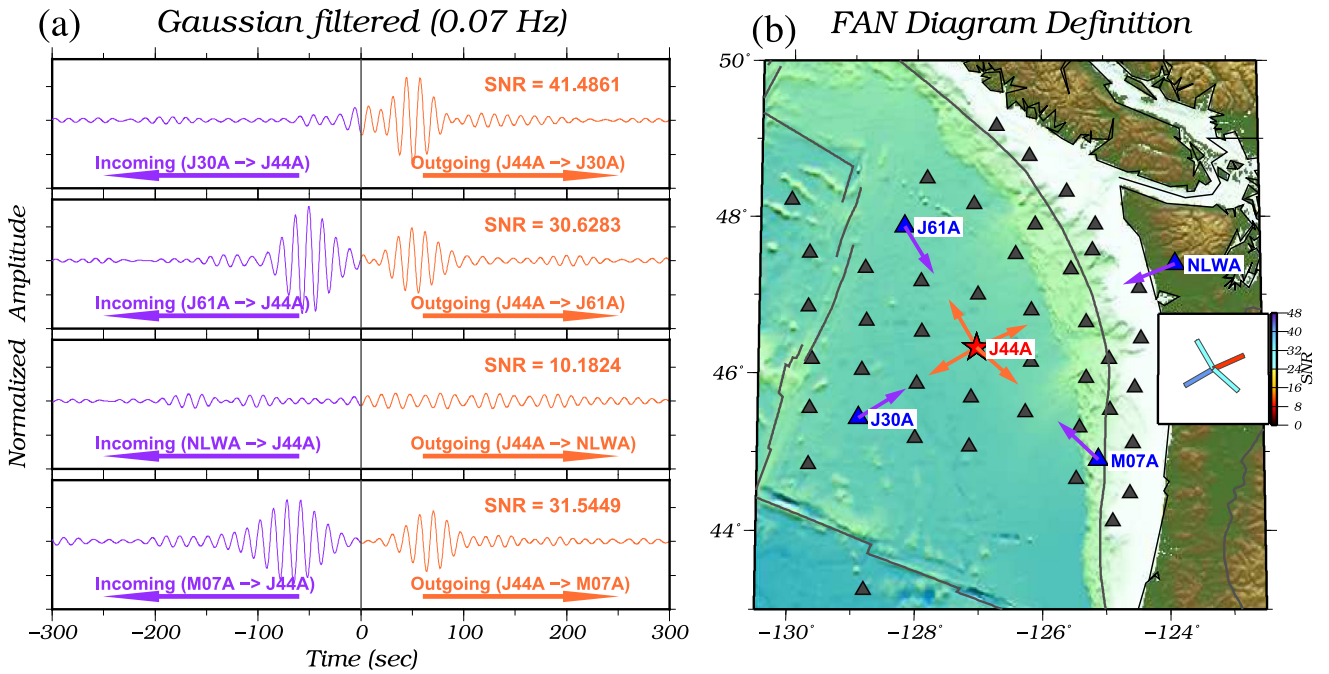

Figure 3. Illustration of the construction of outgoing SNR maps, called fan diagrams. (a) Cross-correlations between OBS station J44A and four nearby stations with a Gaussian filter applied around 0.07 Hz (primary microseism). The positive correlation lags relate to outgoing waves from station J44A, coloured orange, and the incoming waves are on the negative correlation lags, coloured blue. The SNR measurements for the outgoing waves at 0.07 Hz are indicated. (b) The locations of the centre station J44A and the four nearby stations are plotted, respectively, as the red star and blue triangles. Orange arrows show the outgoing wave propagation directions and are assigned to the centre station, whereas the blue arrows are the incoming wave directions and are assigned to the nearby stations. Only outgoing SNRs are presented and are summarized using 'fan diagrams' as exemplified by the inset diagram on the right. The SNR is plotted as same-length coloured bars pointing in the direction of the interstation azimuth (in the direction of wave propagation away from the source) such that blue colours indicate a higher SNR than red colours.

(normalizing to an interstation distance of 150 km) and only use stations within 300 km of the central station. We also normalize all time-series lengths (to 180 d) by assuming that SNR increases as the square root of time. We average the SNRs for the outgoing waves in overlapping 20° azimuth bins and weight them by distance using a spatial Gaussian function with a half width of 150 km which effectively weights up SNR measurements from stations that are close to one another. Note, in a fan diagram, bars point away from sources of ambient noise. A blue bar means that there is strong microseism noise propagating in the direction to which the bar points. A red bar means that little noise propagates in the direction of the bar.

The principal observations of this paper are presented in Figs 4 and 5, which display fan diagrams for the primary and secondary microseisms, respectively, averaged in specified period bands and over the entire time-series length. These results are averaged spatially for each month and are displayed in Fig. 6 to highlight the monthly variation of the SNR of ambient noise as well as its azimuthal content and how it varies between continental and oceanic stations in the two microseism bands. A discussion of the content of these diagrams along with implications for potential source regions for both microseism bands is presented in Section 3.

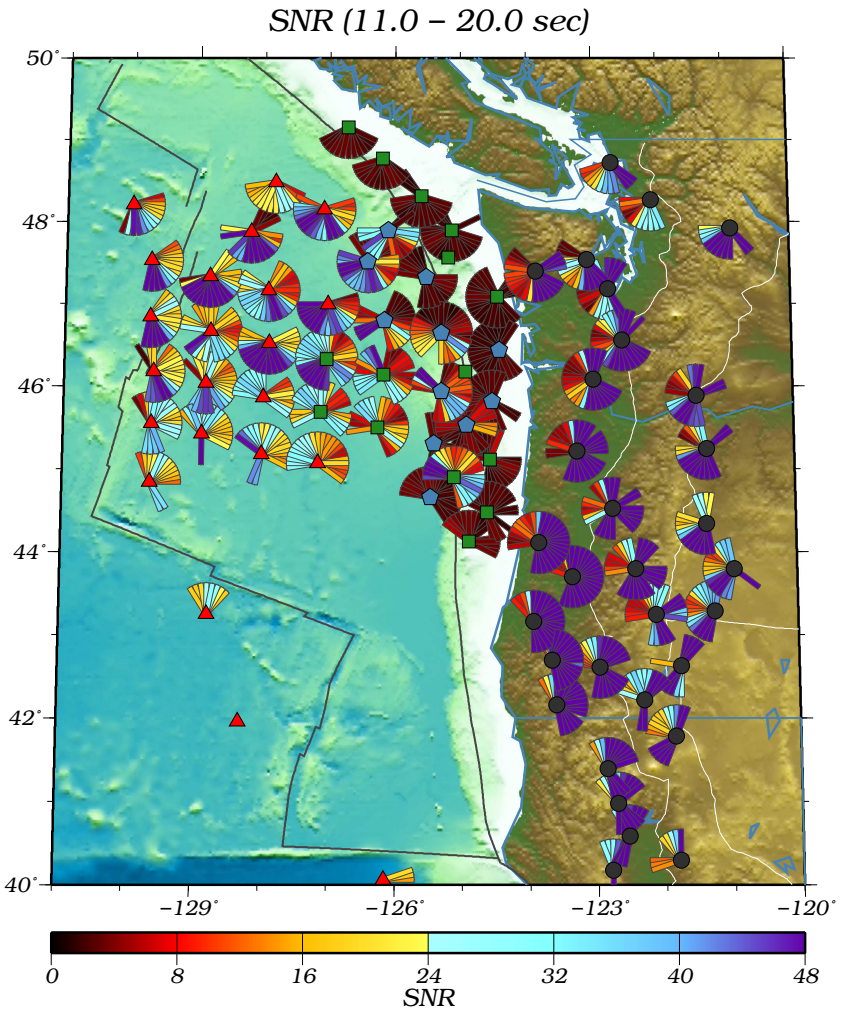

Figure 4. The principal measurements in the paper are presented here and in Fig. 5. Fan diagrams (see Fig. 3 for definition) of outgoing wave amplitudes are plotted at each station for the primary microseism band (11–20 s period). Cooler colours represent higher SNR and point in the direction of propagation (away from the source).

3 THE STRENGTH AND DIRECTIONALITY OF AMBIENT NOISE: OBSERVATIONS

We discuss here the observations with which we will address the questions that motivate this paper by describing the SNR level, the seasonal variation, and the azimuthal content of ambient noise. In doing so, we distinguish between the primary and secondary microseisms as well as continental and oceanic stations where appropriate.

To investigate the directional dependence of microseismic noise in the study area, the stations are grouped spatially into the OBS stations, the northern continental stations (with latitudes above 44°), and the southern continental stations. The spatially averaged SNR within each of the three station groups in the primary and the secondary microseism bands are shown in Fig. 6 as a function of month of observation from December 2011 to May 2012. The SNR curves are plotted with cooler colours indicating the northern winter months and warmer colours indicating the northern spring months. Azimuth is defined clockwise from north so that 0° denotes a wave propagating to the north, 90° is for a wave propagating to the east, and so on.

3.1 Signal level

(1) Ambient noise has a higher SNR on continental than on oceanic stations in both the primary and secondary microseism bands. This is presumably due to higher local noise levels at the oceanic stations, which are incompletely isolated from ocean bottom currents and other sources of local noise (Figs 4–6).

(2) Across the JdF plate, the SNR decreases towards the continent, which we believe results from higher local noise levels in shallower waters. This could be caused either by surface gravity waves coupling to the solid earth or ocean bottom currents that are stronger in shallower water. The SNR being lower in the primary than in the secondary microseism band is consistent with surface gravity waves as the primary cause, as they are expected to be stronger in the primary band (Figs 4–6).

3.2 Seasonal variability (winter–spring)

(1) For most azimuths on both continental and oceanic stations, ambient noise is stronger in the winter than in the spring months. For azimuths between 0 and 90°, however, ambient noise is observed to

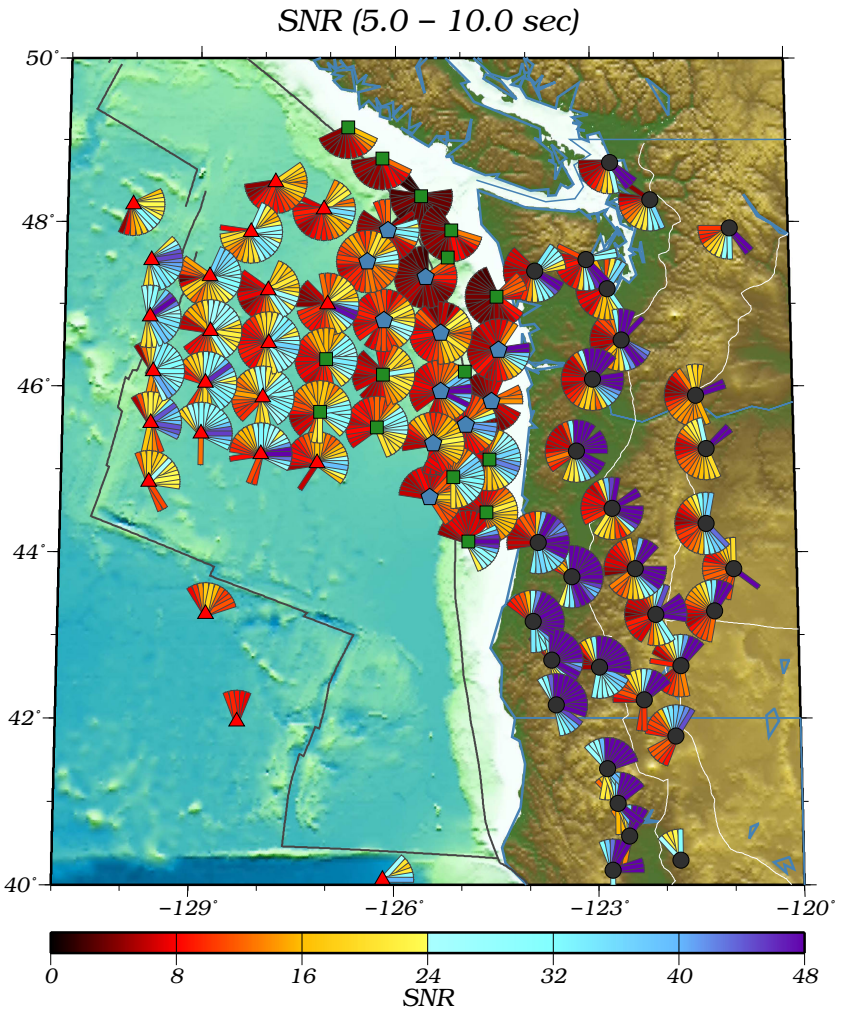

Figure 5. Same as Fig. 4, but for the secondary microseism band (5–10 s period).

be stronger during spring months, or at least more homogeneous in time (Fig. 6).

(2) The azimuthal content of ambient noise changes less over time in the secondary microseism than in the primary microseism band (Fig. 6).

3.3 Azimuthal content

In each of the six diagrams shown in Fig. 6, ambient noise SNR peaks at three to four azimuths as marked by colour-coded arrows. In each microseism band separately, peaks marked by arrows with the matching colour correspond to waves that are potentially from the same source region as will be discussed later and illustrated with Figs 7–10. Note that the yellow and red arrows for the secondary microseisms aim to mark the range over which the signal is the strongest instead of pointing to individual peaks as in the case of the primary microseisms. The back-projected paths and the potential source locations of these peaks will be discussed in Section 4, following.

(1) Ambient noise appears to propagate in all directions (SNR $>$ 5) at both oceanic and continental stations in both microseism bands (Fig. 6).

(2) The red, green and blue arrows in the primary microseism band as well as the red and green arrows in the secondary microseism band mark the azimuths with stronger noise during the winter months, while the yellow peaks in both period bands mark stronger noise during the spring months (Fig. 6).

(3) For the secondary microseism, the azimuthal distribution of ambient noise is temporally and spatially stable for both the OBS and continental stations. The strongest energy is observed continuously in the azimuth range between the red and the yellow arrows, which is associated with waves propagating generally to the east (Figs 6d–f). The green peak is not observed on OBSs and is much smaller in SNR compared to the other two peaks.

(4) For the primary microseism, the four peaks marked by arrows are well separated azimuthally. The directionality of the green and yellow arrows are stable across the three station groups, while the azimuth marked by the red arrows rotates by 15–30° between station groups. The blue peak is observable only on the OBS stations and the southern continental stations (and might be merged with another peak on the northern continental stations) and rotates by more than 140° when observed on the two station groups (Fig. 6).

4. DISCUSSION

Four questions motivate this paper, which we now discuss based on the observations presented in the earlier sections.

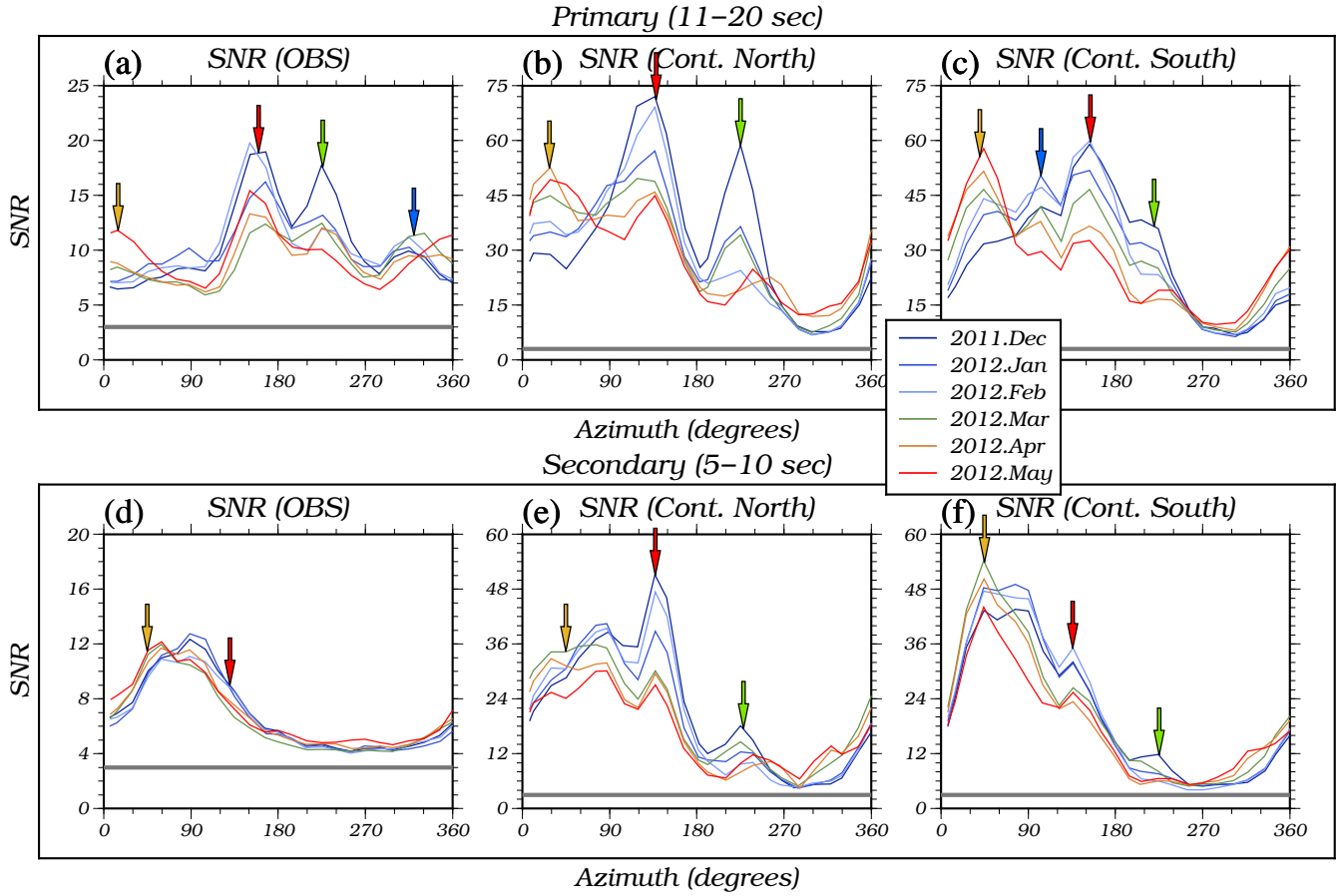

Figure 6. Monthly azimuthal variation of SNR summarizing results in Figs 4 and 5 across the OBS stations (a, d), the continental stations north of 44°N (b, e) and the continental stations to the south (c, f). Results in the primary microseism band (11–20 s) are shown in the top row and the secondary microseism band (5–10 s) in the bottom row. The SNRs measured for each month are plotted with different colours where cooler colours indicate winter months and warmer colours indicate spring months. Grey lines indicate the noise level (SNR = 3). Azimuth is defined clockwise from north so that 0° means propagation to the north, 90° is propagation to the east, and so on. Note that vertical scales differ because SNR is higher for continental than oceanic stations and in the primary microseism than in the secondary microseism bands. For each period band, the primary peaks observed in each of the three diagrams are marked with colour-coded arrows where the same colour across the diagrams may be due to the same noise source.

4.1 Are the primary and secondary microseisms generated at the same locations?

As shown in Fig. 6 and as is illustrated further in Figs 7–10, ambient noise is much different in the primary and secondary microseism bands, both in its azimuthal content and seasonal variation. The propagation of the secondary microseism, both on the continent and within the ocean, is principally eastward and displays little seasonal variation. In contrast, the azimuthal content of the primary microseism on the JdF plate and the northern and southern parts of the continent differ from one another. The azimuthal content of ambient noise varies over time on the continent, with stronger propagation to the southeast and southwest during the winter and to the northeast during the summer. These observations imply well separated locations of generation of the primary and secondary microseisms. As discussed further below, the secondary microseism appears to be generated far from the observing networks, in the open ocean of the northern Pacific, and the primary microseism appears to be derived both locally, in the shallower waters of the northeastern Pacific, and distantly, possibly from locations over broad regions of the Pacific and northern Atlantic Oceans.

4.2 Are ambient noise signals generated in deep water of the North Pacific?

The principal direction of ambient noise in the secondary microseism band is generally to the east, as observed both in the ocean and on the continent and for all months considered. Fig. 7(d) illustrates this by back-projecting the wave propagation paths for the red, green, and yellow peaks shown in Figs 6(d)–(f). Paths with the same colour are almost parallel to each other in Fig. 7(d), indicating distant source locations, although the mean SNR is considerably higher on the continent. As shown in Figs 7(a)–(c), strong time-averaged energy is observed continuously between the red and the yellow arrows and the azimuthal content is similar on the continent and in the ocean, indicating that the source region(s) are likely to be the same and distant from the observing points.

Fig. 8 presents great circle paths back-projected from the OBS locations on a larger area map. Azimuths between the red and yellow arrows (~45–130°) from Fig. 7 are indicated with black lines. The strongest observed signal, which occurs at wave propagation azimuths around 120° (near the red arrows), agrees well with the source regions hypothesized by Gerstoft *et al.* (2008) and

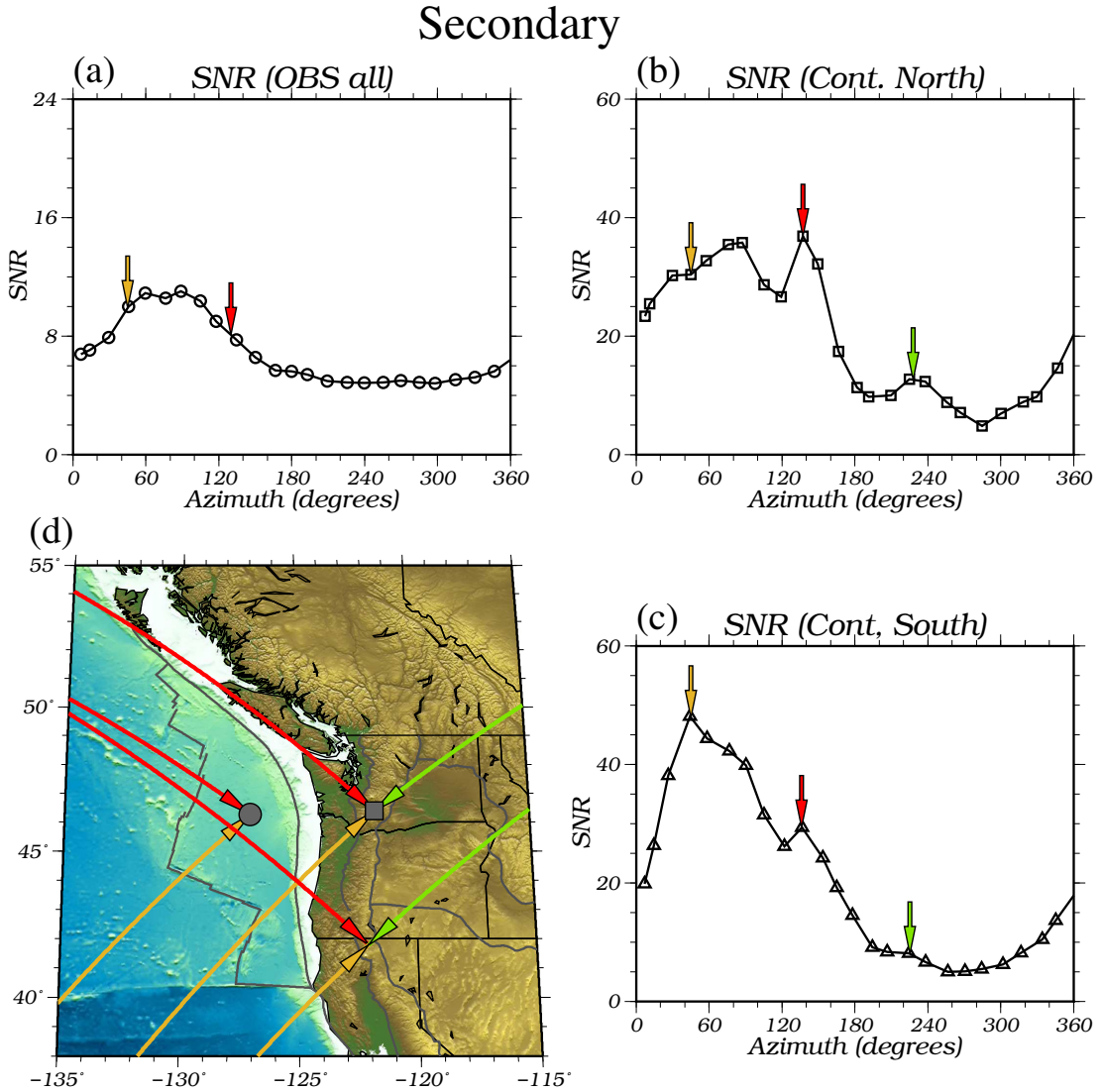

Figure 7. The azimuthal variations of SNRs averaged across all months for the secondary microseisms are shown (a) for OBS stations, (b) for continental stations to the north of 44°N and (c) for continental stations to the south. The same principle SNR peaks as marked in Figs 6(d)–(f) are marked with arrows in three different colours. The back-projected great circle paths of these three sets of peaks are plotted in (d) with the same colours.

Landès *et al.* (2010) for body waves (marked with orange and yellow ellipses). The second strongest signal in the secondary band occurs at azimuths around 60° (near the yellow arrows), which is outside of these regions. However, Kedar *et al.* (2008) predicts a diffuse intense region of wave–wave interaction in the northern Pacific Ocean (marked with a green ellipse), which is weakened after multiplying by the microseismic excitation potential. Landès *et al.* (2010) also observed a weaker source region in the central Pacific Ocean (marked with a yellow dashed ellipse in Fig. 8). It is possible that the enhanced signal near 60° azimuth that we observe is generated in these regions.

The seasonal characteristics of the 60° (near the yellow arrows) and 120° (near the red arrows) azimuthal peaks (Figs 6d–f) are different from one another. The 60° signal is slightly stronger during the spring months while at 120° the signal is strongest for the winter months. This is consistent with the assumption that the energy propagating at 120° is produced by storm activities over the deep North Pacific Ocean, which is stronger during the northern winter months (Gerstoft *et al.* 2008; Landès *et al.* 2010), while the 60° energy is produced over the Central Pacific Ocean, which is expected to have less seasonal variability.

The strongest secondary microseism source in the Northern Hemisphere during the winter months is predicted to be near the southern tip of Greenland by Kedar *et al.* (2008) and Ardhuin *et al.* (2011). The propagation direction of waves from this source agrees well with the observed green peaks on Figs 6(e) and (f) and Figs 7(b) and (c) with the propagation direction shown in Fig. 7(d). Peaks with similar azimuthal contents are observed in the primary microseism band (Fig. 9) with their back-projected great circle paths plotted in Fig. 10.

Overall, the strength of the secondary microseism we observe is relatively stable over time with winter months being slightly stronger. Earlier studies have shown similar seasonality for the secondary microseisms but, in some cases, with the strength being less stable over time (e.g. Gerstoft *et al.* 2008; Kimman *et al.* 2012). Two factors may have contributed to this difference: (1) geographical factors in different study regions, such as the storm activities and bathymetry distribution, could have affected the observed

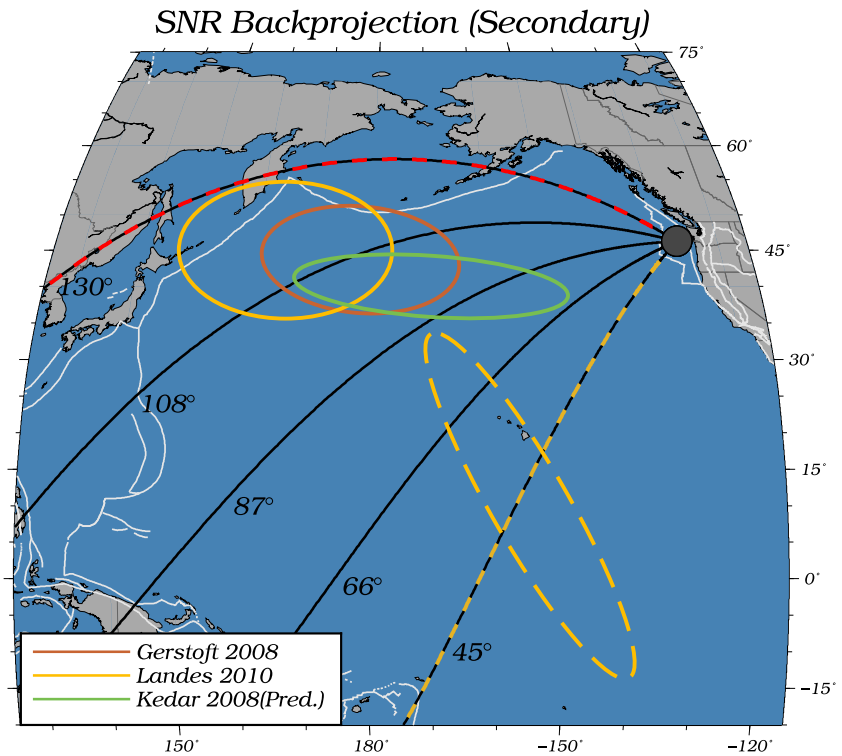

Figure 8. Possible source regions for the secondary microseisms. Great-circle lines are plotted at azimuths of 45° (yellow dash), 66°, 87°, 108° and 130° (red dash). Yellow and red dashed lines correspond exactly to the yellow and red arrows in Figs 6 and 7. Orange and yellow solid ellipses indicate the source regions inferred by Gerstoft *et al.* (2008) and Landès *et al.* (2010) for body waves in ambient noise. The yellow dashed ellipse indicates a weaker source region from Landès. The green ellipse indicates the intense region of wave–wave interaction predicted theoretically by Kedar *et al.* (2008). (The source regions marked here are approximate.)

signal strength, and (2) the strength of the secondary microseisms observed through ambient noise cross-correlations, as in our study, is homogenized by the pre-cross-correlation normalizations and the time averaging processes.

In summary, our observations are consistent with deep water generation of the secondary microseism perhaps coincident with the regions of body wave excitation inferred by Gerstoft *et al.* (2008) and Landès *et al.* (2010). The azimuthal content of the primary microseism is more complicated and not as easily explained with a small set of deep water source regions as the secondary microseism. In fact, the primary microseism appears to be generated in different areas than the secondary microseism. We discuss the possible source regions of the primary microseism in the next subsection.

4.3 Are ambient noise signals generated locally in shallow waters on the JdF plate and its surroundings?

Fig. 9 presents time-averages of the four primary microseism peaks observed across the three station groups and their back-projected paths. A more complicated picture emerges than for the secondary microseism, including what we interpret as evidence for both distant and relatively local sources. Four observations are particularly noteworthy.

(1) The green arrows in Fig. 9(d) correspond to directions similar to those observed in the secondary microseism band (Fig. 7d). This signal is probably caused by a North Atlantic source, as the back-projection in Fig. 10 (green region) indicates. However, the source region or regions are too distant for us to determine if the primary and secondary microseisms are being generated in the same or different locations.

(2) The yellow arrows in Fig. 9(d) indicate a Pacific source. The peak at the OBS stations (Fig. 9a) is much weaker than for the continental stations but is well observed in Fig. 6(a) in the spring. Because the yellow arrows in Fig. 9(d) are not parallel to one another, this source may be considered to be relatively close. However, because of the relatively low SNR level, the azimuthal content for these peaks is not precise and, as Fig. 6 illustrates, this wave is stronger in the northern spring than in the winter months. Therefore, we believe that it is likely that this source is distant and in the Southern Hemisphere. Fig. 10 presents the back-projection of the azimuths observed, illustrating that a broad area of the southern Pacific is potentially consistent for generating these signals. We cannot determine if this is a deep water or shallow water source region.

(3) The three red paths in Fig. 9(d) intersect in the shallow water regions to the northwest of the JdF plate, and we believe that these peaks in the primary microseism band are generated relatively locally in shallow waters. The intersection point is approximate and should not be interpreted to convey the source location accurately, but our estimate lies near the coast of British Columbia and Graham Island. The water depth in much of this area is shallower than 50 m and shallower still near Graham Island. The wavelength of the deep water gravity wave, given by the Airy wave theory ($\lambda = gT^2/2\pi$, where g is the gravitational acceleration and T is the period), is between 190 and 620 m for the primary microseism band (11–20 s). Thus, the water depth within this area satisfies the theoretical requirement for ocean wave energy to transfer into the solid earth by direct coupling, which mostly occurs where the water depth is

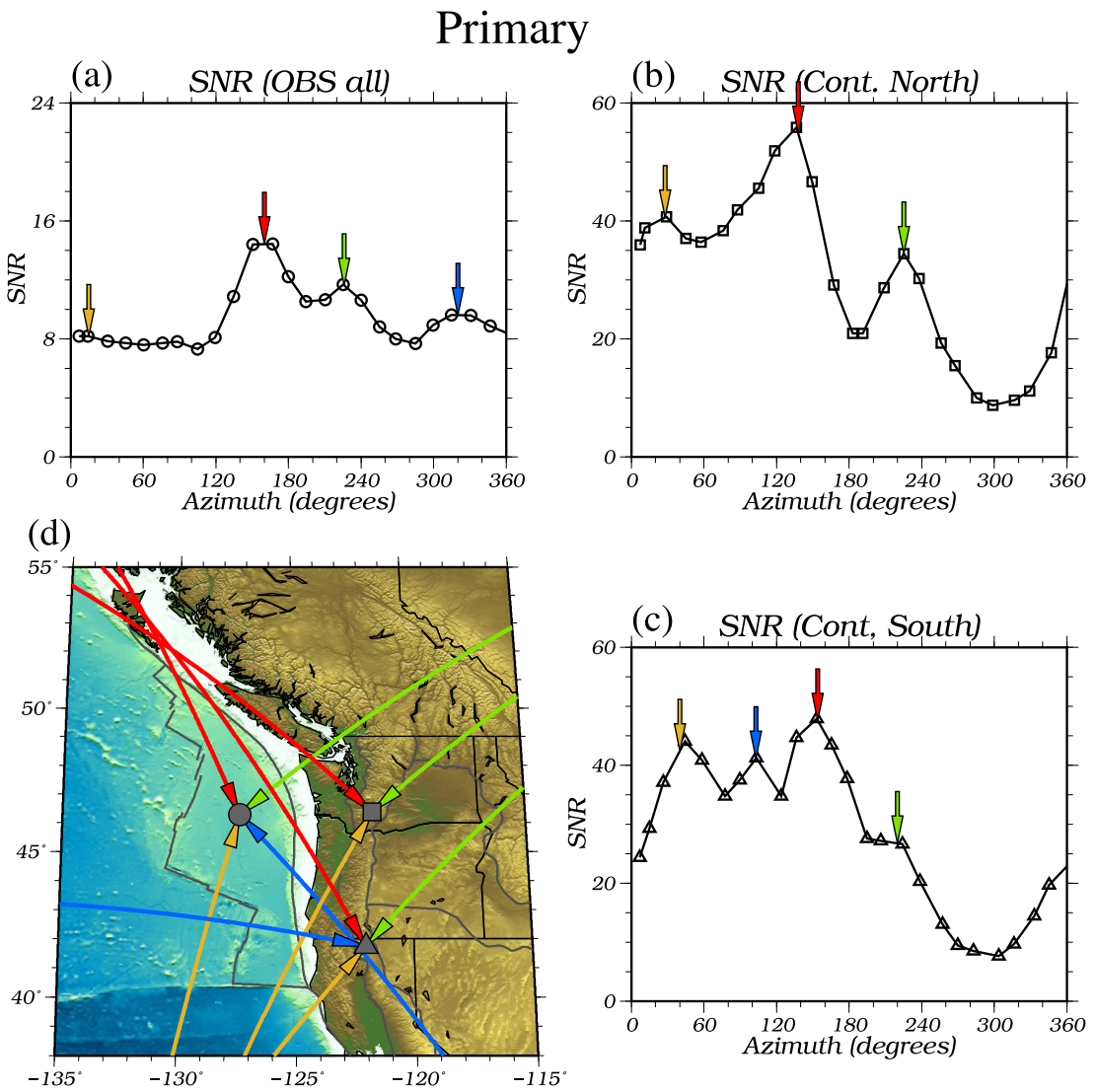

Figure 9. Similar to Fig. 7, but for the primary microseism.

within 1/4 wavelength of the deep water gravity wave (Hasselmann 1963; Bromirski & Duennebier 2002).

(4) The amplitude of the curves near the blue arrows are weaker compared to near the red arrows, the peak is not observed on the northern continental stations and its directionality is complicated, as seen in Fig. 9(d). We believe that this peak also originates locally in shallow waters, probably off the southern Oregon coast. Even though this signal is not obviously evident in the azimuthal plots such as those in Fig. 9, it may be indicated by precursory signals, which we discuss now.

In addition to the SNR of the observed surface wave signals, clear systematic precursory arrivals are observed for many station pairs. These observations produce complementary evidence about the location of some microseism sources. Fig. 11 presents an example of such a precursory signal on the cross-correlation of the station-pair J42A–I05D. Strong precursors appear near zero time on both the broadband and the primary microseism signals, but disappear when filtered into the secondary microseism band. Thus, such precursors are nearly entirely in the primary band. (The time and duration of the precursor observed on this station pair is consistent with the source location identified by the blue ellipse in Fig. 12a.) Systematic observations of precursors from this source and two other source locations are presented in Fig. 12 with two cross-correlation record sections centred at the continental stations B05D and I05D. All presented cross-correlations are between OBS and continental stations and are filtered in the period band 0.06–0.085 Hz (within the primary microseism band) where the precursory signals are particularly strong.

The fact that the precursory signals appear in a systematic way in these record sections indicates that they are generated by localized sources and more than one such source region is needed. To test this conclusion we assume three potential source regions as marked by red, green and blue ellipses in Fig. 12(a), off the coast of northern British Columbia (red), near Vancouver Island (green) and off the southern Oregon coast (blue). We then predict the arrival times of the precursory signals that would be generated on cross-correlations of ambient noise based on a simple group velocity model as indicated by the background colour in Fig. 12(a) (group velocity, ocean: 3.4 km s^{-1}, continent: 2.5 km s^{-1}), which has been determined by averaging the measurements made on oceanic and continental paths in this region. The red, green and blue ellipses in the record sections (Figs 12b and c) indicate the predicted arrival times with colours associated with the three source regions. Note that the

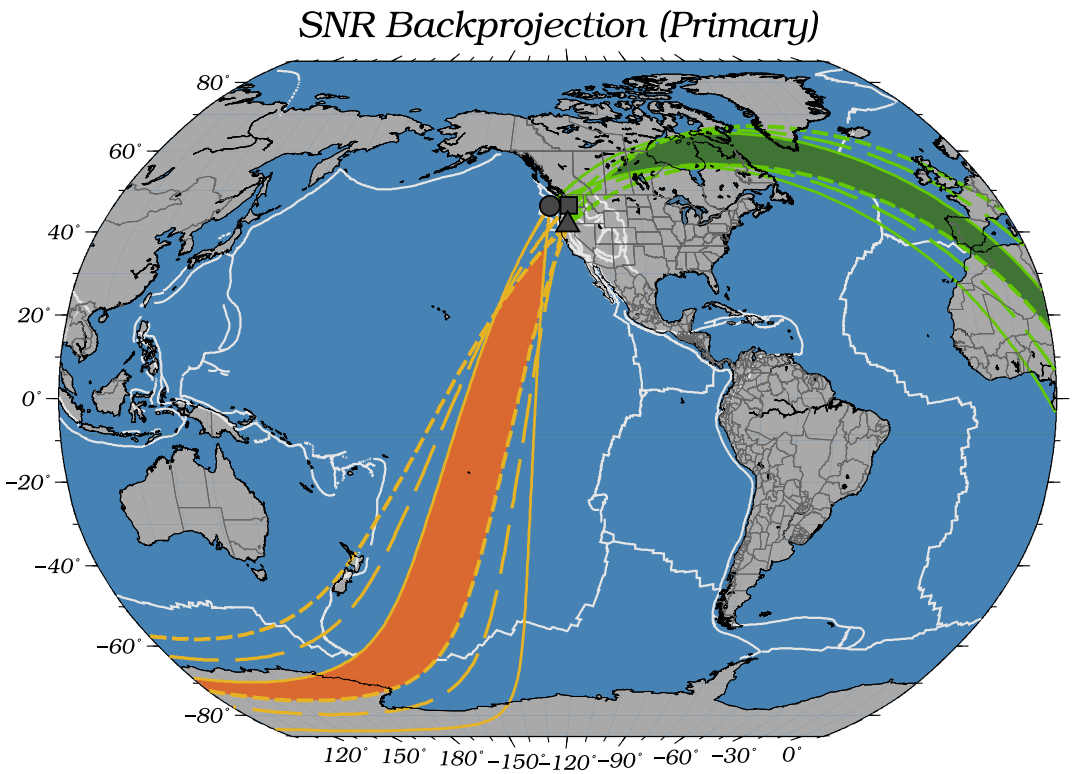

Figure 10. Possible source regions for the higher amplitudes near the green and yellow arrows shown in Figs 6 and 9. The azimuth ranges of the SNR peaks are shown, respectively, with solid lines for OBS stations, long dashed lines for continental stations in the north, and short dashed lines for continental stations in the south. The azimuth ranges for the green arrows are chosen to be 218–234° on the OBSs, 217–233° on the northern continental stations, and 212–228° on the southern continental stations. The azimuth ranges for the yellow arrows are chosen to be 5–30° on the OBSs, 15–40° on the northern continental stations, and 20–45° on the southern continental stations. The peak near the yellow arrows is wider in azimuth as shown in Figs 6(a)–(c) and 9, thus the choices of wider ranges. The overlapping regions are coloured dark green and orange for the green and yellow arrows, respectively.

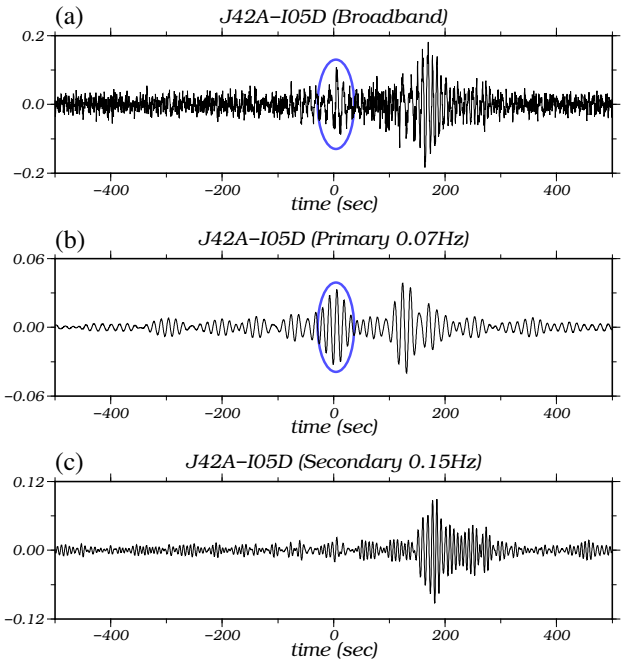

Figure 11. Example of precursory signals observed on ambient noise cross-correlations for station pair J42A–I05D. (a) Broadband cross-correlation. (b) Cross-correlation filtered in the primary microseism band. (c) Cross-correlation filtered in the secondary microseism band. The precursory signal window is marked with a blue ellipse in each diagram and is associated with the blue source region of Fig. 12(a).

duration of the predicted precursory arrival window is a function of the geometrical relation between the interstation path and the spatial extent of the source region. A larger source region tends to produce a larger precursory window, on average, but would not cause a wider window if the sources align with a hyperbola whose foci are the two station locations. The orange bands indicate arrival times of the fundamental Rayleigh waves in the cross-correlations, the non-precursory signals, predicted with a group velocity of 3 km s^{-1}.

The predictions match most of the observed precursory signals regardless of the fact that the group speed model is an over simplification. On cross-correlations centred at station I05D, which is located in Central Oregon, the strongest precursory arrivals match predictions from the blue source region. Cross-correlations centred on station B05D, on the other hand, are more sensitive to energy from the red and green sources due to proximity. This suggests that the signals produced in these source regions are probably scattered and the direct arrival decays quickly with distance. The locations of the red and blue source regions agree well with the azimuthal content of the fundamental surface waves as shown in Fig. 9. The green source region, however, is not easily identified through its azimuthal dependence as it is possibly merged in azimuth with peaks from other source regions. The observed shallow water source locations and the discontinuity of sources along the coastline are consistent with earlier studies that have argued that the primary microseism sources are limited to certain coastal locations (e.g. Cessaro 1994; Bromirski & Duennebier 2002).

A large number of small earthquakes (magnitude 3–4) occurred near Graham Island and on the explorer plate, along the Blanco fracture zone, the Gorda Ridge, and the Mendocino fracture zone in the

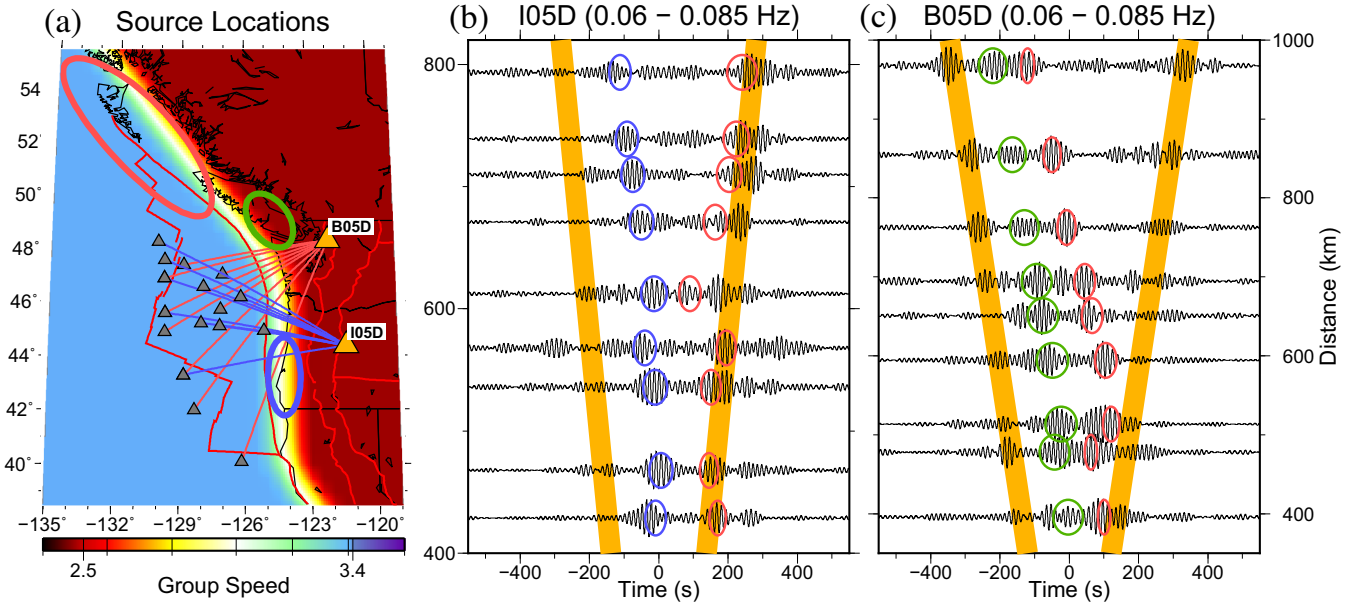

Figure 12. (a) The locations of the three potential local source regions are indicated with red, green, and blue ellipses. Background colour shows the group speed model used in predicting the precursory signals produced by these sources. The two centre stations B05D and I05D are marked with orange triangles. Paths between station pairs that are shown in (b) and (c) are indicated with blue and red lines, respectively. (b) The record section of example cross-correlations between the centre station I05D and 9 OBSs. Blue ellipses indicate the predicted precursory arrival times from the blue potential source location shown in (a). Yellow lines indicate the predicted fundamental mode Rayleigh wave arrival times with a group speed of 3 km s^{-1}. (c) Similar to (b), cross-correlations centred on stations B05D are shown. Red and green ellipses are associated with the red and green potential source locations identified in (a).

time period in which our cross-correlations are computed. Therefore, in principal, some of the precursory signals we observe may be earthquake generated. We believe, however, that this is not the case for two principal reasons. (1) The precursory signals we observe are strongest in the primary microseism band and are largely not present in the secondary microseism band. This is opposite of what would be expected if small local earthquakes were the source of the precursory arrivals as such earthquakes would generate stronger signals at shorter periods. (2) The precursory signals associated with the blue ellipses on the record sections are fit far better if we set the source region to be along the southern Oregon coastline rather than shifting it westward where the majority of small earthquakes occurs. Nonetheless, the amplitudes of the precursory signals, especially those associated with the blue source region, are affected by surrounding small earthquakes. 'Precursor-to-Noise Ratios' (PNRs) decay with the source-station distances in the expected way for the red and green source regions but for the blue source region do not show a clear decay.

As with the azimuthal content of the Rayleigh waves in the cross-correlations, the use of the arrival times of precursory signals is not a highly accurate means to determine source locations. Therefore, source regions other than the three discussed may (and probably do) exist. An example of signals that are not accounted for can be seen in Fig. 12(b) on the positive lags where signals with large amplitudes arrive after the fundamental mode Rayleigh wave. These 'post-cursory' signals could arise either due to multiple scattering of surface wave energy or where large gradients exist in the local group speed structure. The ocean–continent boundary is a good example of such a structure and the presence of the 'post-cursory signals' in our observations may indicate source generation along the coastline farther to the northwest of the study area near, for example, the Gulf of Alaska. A formal analysis of the post-cursors, however, is beyond the scope of this paper. Moreover, the Rayleigh wave arrivals could be merged with the precursory signals produced by these localized sources, such as those shown in Fig. 12(b). Thus, additional denoising processing may be needed for studies aiming to investigate the shallow velocity structure in this region.

In conclusion, local primary microseism sources are indicated by observations from the azimuthal dependence of the fundamental mode Rayleigh wave SNRs as well as observations from precursory signals. The strongest local generation region is observed to the northwest of the JdF plate near the coast of British Columbia perhaps near Graham Island. Two weaker generation regions are observed in shallow waters near the western United States coastline, one near Vancouver Island and another along the coastline of southern Oregon.

4.4 Does the ambient noise wavefield extend from the oceanic to the continental parts of the study region?

To show that the deep-water generated microseisms observed in this study do propagate onto the continent, we present in Fig. 13 five example cross-correlations along the west–east path between OBS stations J47A, J37A, J35A and J33A and continental station I05D. Three of these are between oceanic stations: J47A–J37A, J47A–J35A and J47A–J33A. The other two are from oceanic to continental stations: J33A–I05D and J47A–I05D. Station J47A is located well out of the shallow water region about 400 km from the coastline where water depth is over 2500 meters. The locations of the five paths are indicated by black arrows in Fig. 13(a) and the positive lags of the corresponding cross-correlations and their FTAN diagrams are presented in Figs 13(b)–(f). The measured group and phase velocity dispersion curves are indicated by white and blue dots, respectively.

On cross-correlations near the JdF Ridge, as shown in Figs 13(b) and (c) for station pairs J47A–J37A and J47A–J35A, clear fundamental mode Rayleigh wave signals are observed in a period range

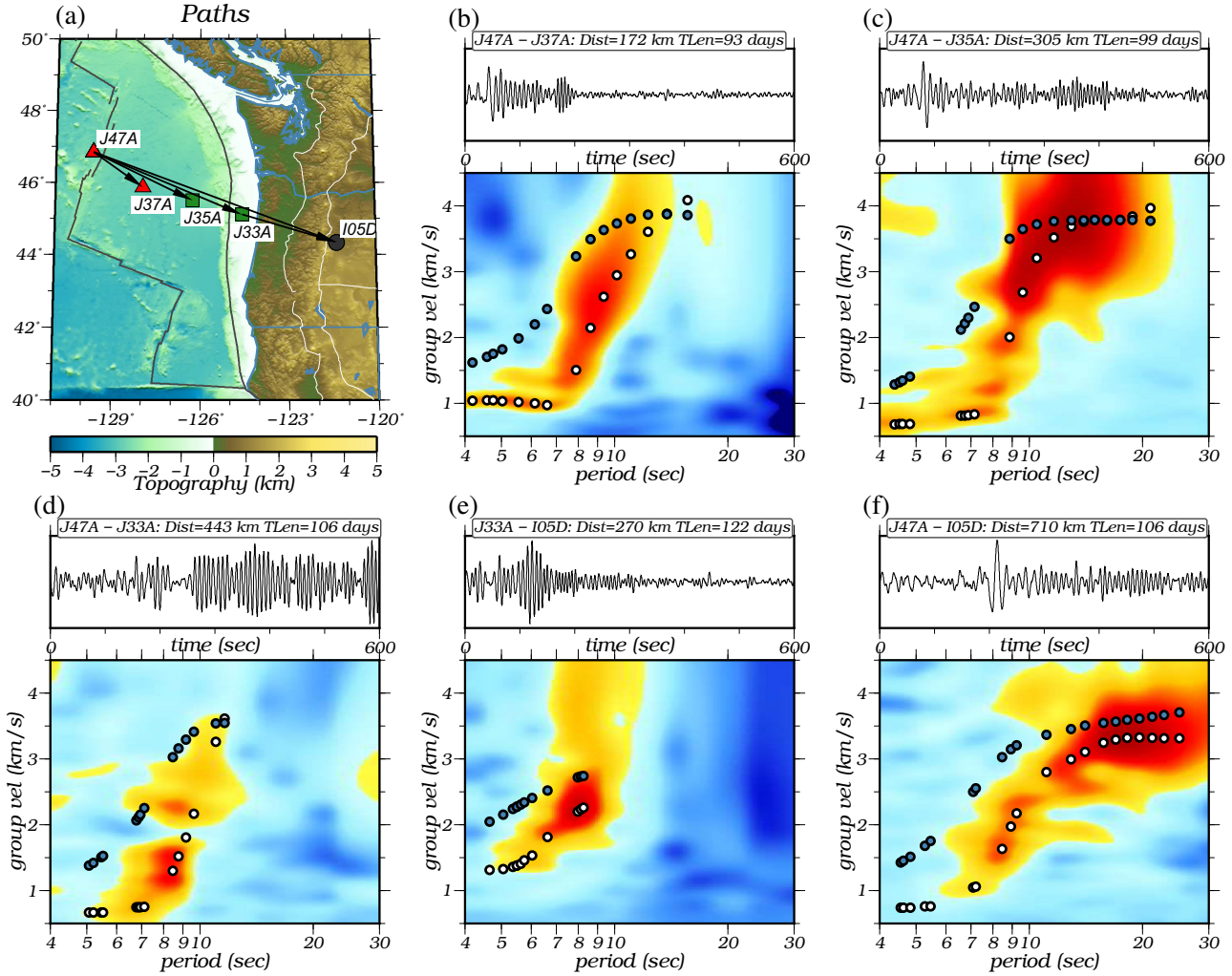

Figure 13. FTAN diagrams for five example paths showing surface waves propagating from the oceanic lithosphere onto the continent. (a) Locations of the paths are plotted with black arrows. The positive lag cross correlations and their corresponding FTAN diagrams are plotted in (b)–(f) for paths J47A–J37A, J47A–J35A, J47A–J33A, J33A–I05D and J47A–I05D, respectively. The measured group and phase speed dispersion curves are shown with white and blue dots, respectively. Only winter months were used to produce the cross-correlations.

that extends to as low as 4 s. Longer period signals (>15 s) are missing from the station pair J47A–J37A, as is often the case for stations that are near to one another, but longer period signals are well observed on stations that are further separated, such as the station pair J47A–J35A. Cross-correlations including stations located in shallow waters near the coastline, however, appear to be much noisier, especially in the primary microseism band. Figs 13(d) and (e) show two examples of such cross-correlations, one on the oceanic side between station pair J47A–J33A and the other on the continental side between station pair J33A–I05D. The contamination is probably from tilting and compliance noise in the shallow ocean as described by Webb & Crawford (1999) and Crawford & Webb (2000). Such noise largely disappears for cross-correlations from deep water to the continent, as shown in Fig. 13(f). Fairly strong fundamental mode dispersion is observed between 5 and 30 s period on the station pair J47A–I05D, although signals in the secondary microseism band appear to be weaker.

We conclude, therefore, that in both the primary and secondary microseism bands, deep-water generated microseisms efficiently propagate onto the continent and are recorded by seismic stations. The shallow water stations appear to be contaminated by strong local noise and denoise techniques (e.g. Webb & Crawford 1999; Crawford & Webb 2000) may be necessary to extract the ambient noise signal in these regions. Below 5 s period, however, no signals are observed between the deep oceanic and continental stations, which is probably due to scattering attenuation (and perhaps anelastic attenuation) at the transition across the continental–shelf boundary as discussed by Bromirski *et al.* (2013).

5 CONCLUSIONS

We investigate the source locations of the primary and secondary microseism signals based on cross-correlations of the vertical components of 61 OBSs located on the JdF plate from the Cascadia Initiative experiment and 42 continental stations situated in the Pacific Northwest near the U.S. coast. Ambient noise observed across the array is much different in the primary and secondary microseism bands, both in its azimuthal content and seasonal variation, indicating different source generation locations.

In the secondary microseism band, the principal signals propagate to the east and display little seasonal variation both on the continent and on the ocean bottom. Observed azimuthal contents are consistent with source generation in deep water of the North Pacific, which is possibly coincident both with the region of body

wave excitation observed by Gerstoft *et al.* (2008) and Landès *et al.* (2010) and with the diffuse intense region of wave–wave interaction predicted by Kedar *et al.* (2008).

In the primary microseism band, the observed azimuthal contents on the JdF plate and the northern and southern parts of the continent arrays differ from one another. Strong seasonal variations are observed in all three regions. Waves propagating to the northeast are stronger during the northern spring, indicating possible distant sources from the south Pacific, while waves propagating to the south and east are stronger during the northern winter months. We infer the existence of local sources from observations of the azimuthal dependence of the fundamental mode Rayleigh wave SNRs as well as observations of precursory signals. The strongest local generation region is inferred to lie to the northwest of the JdF plate near the coast of British Columbia, perhaps near Graham Island. Two weaker generation regions are observed in shallow waters near the western U.S. coastline, one near Vancouver Island and another along the southern coastline of Oregon.

The observed locations of generation of the primary and secondary microseisms agree well with the theories proposed by Longuet-Higgins (1950) and Hasselmann (1963). The secondary microseisms are dominated by deep-water sources in the northern Pacific, which are likely to be due to non-linear wave–wave interaction either with wind waves or between independent wave systems over the deep Pacific Ocean. In contrast, primary microseisms are derived significantly from the local shallow waters of the eastern Pacific, which suggest direct coupling of ocean gravity waves into the shallow ocean bottom as the generation mechanism. Additionally, primary microseism energy appears to derive from distant sources of unknown origin in the North Atlantic and in the Central to Southern Pacific.

Finally, high quality ambient noise empirical Green's functions derived from the ambient noise cross-correlations are observed between continental stations and deep water OBSs, which illustrates that deep water generated seismic surface waves do efficiently propagate onto the continent and are well recorded by continental seismic stations, at least above 5 s period.

ACKNOWLEDGEMENTS

The authors appreciate constructive reviews from an anonymous reviewer and Jeannot Trampert, which helped to improve this paper. The authors are grateful to the Cascadia Initiative Expedition Team for acquiring the Amphibious Array Ocean Bottom Seismograph data and appreciate the open data policy that made the data available shortly after they were acquired. The facilities of IRIS Data Services, and specifically the IRIS Data Management Center, were used for access to waveforms, related metadata, and/or derived products used in this study. IRIS Data Services are funded through the Seismological Facilities for the Advancement of Geoscience and EarthScope (SAGE) Proposal of the National Science Foundation under Cooperative Agreement EAR-1261681. This work utilized the Janus supercomputer, which is supported by the National Science Foundation (award number CNS-0821794), the University of Colorado Boulder, the University of Colorado Denver and the National Center for Atmospheric Research. The Janus supercomputer is operated by the University of Colorado Boulder.

REFERENCES

Ardhuin, F., Stutzmann, E., Schimmel, M. & Mangeney, A., 2011. Ocean wave sources of seismic noise, *J. geophys. Res.,* **116**(C9), doi:10.1029/2011JC006952.

Bensen, G.D., Ritzwoller, M.H., Barmin, M.P., Levshin, A.L., Lin, F., Moschetti, M.P., Shapiro, N.M. & Yang, Y., 2007. Processing seismic ambient noise data to obtain reliable broad-band surface wave dispersion measurements, *Geophys. J. Int.,* **169**(3), 1239–1260.

Bromirski, P.D. & Duennebier, F.K., 2002. The near-coastal microseism spectrum: spatial and temporal wave climate relationships, *J. geophys. Res.,* **107**(B8), 2166, doi:10.1029/2001JB000265.

Bromirski, P.D., Duennebier, F.K. & Stephen, R.A., 2005. Mid-ocean microseisms, *Geochem. Geophys. Geosyst.,* **6**(4), Q04009, doi:10.1029/2004GC000768.

Bromirski, P.D., Stephen, R.A. & Gerstoft, P., 2013. Are deep-ocean-generated surface-wave microseisms observed on land?, *J. geophys. Res.: Solid Earth,* **118**(7), 3610–3629.

Cessaro, R.K., 1994. Sources of primary and secondary microseisms, *Bull. seism. Soc. Am.,* **84**(1), 142–148.

Chen, Y.-N. *et al.*, 2011. Characteristics of short period secondary microseisms (SPSM) in Taiwan: the influence of shallow ocean strait on SPSM: SPSM excitations in offshore Taiwan, *Geophys. Res. Lett.,* **38**(4), doi:10.1029/2010GL046290.

Crawford, W.C. & Webb, S.C., 2000. Identifying and removing tilt noise from low-frequency (<0.1 Hz) seafloor vertical seismic data, *Bull. seism. Soc. Am.,* **90**(4), 952–963.

Gerstoft, P., Shearer, P.M., Harmon, N. & Zhang, J., 2008. Global P, PP, and PKP wave microseisms observed from distant storms, *Geophys. Res. Lett.,* **35**(23), doi:10.1029/2008GL036111.

Gu, Y.J. & Shen, L., 2012. Microseismic noise from large ice-covered lakes?, *Bull. seism. Soc. Am.,* **102**(3), 1155–1166.

Gu, Y.J., Dublanko, C., Lerner-Lam, A., Brzak, K. & Steckler, M., 2007. Probing the sources of ambient seismic noise near the coasts of southern Italy, *Geophys. Res. Lett.,* **34**(22), doi:10.1029/2007GL031967.

Harmon, N., Rychert, C. & Gerstoft, P., 2010. Distribution of noise sources for seismic interferometry, *Geophys. J. Int.,* **183**(3), 1470–1484.

Hasselmann, K., 1963. A statistical analysis of the generation of microseisms, *Rev. Geophys.,* **1**(2), 177–210.

Haubrich, R.A. & McCamy, K., 1969. Microseisms: coastal and pelagic sources, *Rev. Geophys.,* **7**(3), 539–571.

Hillers, G., Graham, N., Campillo, M., Kedar, S., Landès, M. & Shapiro, N., 2012. Global oceanic microseism sources as seen by seismic arrays and predicted by wave action models, *Geochem. Geophys. Geosyst.,* **13**(1), doi:10.1029/2011GC003875.

Kedar, S., 2011. Source distribution of ocean microseisms and implications for time-dependent noise tomography, *Comptes Rendus Geosci.,* **343**(8), 548–557.

Kedar, S., Longuet-Higgins, M., Webb, F., Graham, N., Clayton, R. & Jones, C., 2008. The origin of deep ocean microseisms in the North Atlantic Ocean, *Proc. R. Soc. Math. Phys. Eng. Sci.,* **464**(2091), 777–793.

Kibblewhite, A. & Ewans, K., 1985. Wave-wave interactions, microseisms, and infrasonic ambient noise in the ocean, *J. acoust. Soc. Am.,* **78**(3), 981–994.

Kimman, W.P., Campman, X. & Trampert, J., 2012. Characteristics of seismic noise: fundamental and higher mode energy observed in the northeast of the Netherlands, *Bull. seism. Soc. Am.,* **102**(4), 1388–1399.

Köhler, A., Weidle, C. & Maupin, V., 2011. Directionality analysis and Rayleigh wave tomography of ambient seismic noise in southern Norway: ambient noise tomography of southern Norway, *Geophys. J. Int.,* **184**(1), 287–300.

Landès, M., Hubans, F., Shapiro, N.M., Paul, A. & Campillo, M., 2010. Origin of deep ocean microseisms by using teleseismic body waves, *J. geophys. Res.: Solid Earth 1978–2012,* **115**(B5), doi:10.1029/2009JB006918.

Levshin, A.L. & Ritzwoller, M.H., 2001. Automated detection, extraction, and measurement of regional surface waves, in *Monitoring the Comprehensive Nuclear-Test-Ban Treaty: Surface Waves,* pp. 1531–1545, Springer.

Lin, F.-C., Ritzwoller, M.H., Townend, J., Bannister, S. & Savage, M.K., 2007. Ambient noise Rayleigh wave tomography of New Zealand, *Geophys. J. Int.,* **170**(2), 649–666.

Lin, F.-C., Moschetti, M.P. & Ritzwoller, M.H., 2008. Surface wave tomography of the western United States from ambient seismic noise: Rayleigh and Love wave phase velocity maps, *Geophys. J. Int.,* **173**(1), 281–298.

Longuet-Higgins, M.S., 1950. A theory of the origin of microseisms, *Phil. Trans. R. Soc. Lond., A: Math. Phys. Sci.,* **243**(857), 1–35.

Miche, R., 1944. *Mouvements ondulatoires de la mer en profondeur constante ou décroissante forme limite de la houle lors de son déferlement, application aux digues maritimes,* Paris.

Moschetti, M.P., Ritzwoller, M.H. & Shapiro, N.M., 2007. Surface wave tomography of the western United States from ambient seismic noise: Rayleigh wave group velocity maps: U.S. surface wave tomography, *Geochem. Geophys. Geosyst.,* **8**(8), doi:10.1029/2007GC001655.

Sabra, K.G., Gerstoft, P., Roux, P., Kuperman, W.A. & Fehler, M.C., 2005. Extracting time-domain Green's function estimates from ambient seismic noise, *Geophys. Res. Lett.,* **32**(3), doi:10.1029/2004GL021862.

Shapiro, N.M., Campillo, M., Stehly, L. & Ritzwoller, M.H., 2005. High-resolution surface-wave tomography from ambient seismic noise, *Science,* **307**(5715), 1615–1618.

Shapiro, N.M., Ritzwoller, M.H. & Bensen, G.D., 2006. Source location of the 26 sec microseism from cross-correlations of ambient seismic noise, *Geophys. Res. Lett.,* **33**(18), doi:10.1029/2006GL027010.

Stehly, L., Campillo, M. & Shapiro, N.M., 2006. A study of the seismic noise from its long-range correlation properties, *J. geophys. Res.: Solid Earth, 1978–2012,* **111**(B10), doi:10.1029/2005JB004237.

Tian, Y., Shen, W. & Ritzwoller, M.H., 2013. Crustal and uppermost mantle shear velocity structure adjacent to the Juan de Fuca Ridge from ambient seismic noise, *Geochem. Geophys. Geosyst.,* **14**(8), 3221–3233.

Tsai, V.C., 2009. On establishing the accuracy of noise tomography travel-time measurements in a realistic medium, *Geophys. J. Int.,* **178**(3), 1555–1564.

Weaver, R., Froment, B. & Campillo, M., 2009. On the correlation of non-isotropically distributed ballistic scalar diffuse waves, *J. acoust. Soc. Am.,* **126**(4), 1817, doi:10.1121/1.3203359.

Webb, S.C. & Crawford, W.C., 1999. Long-period seafloor seismology and deformation under ocean waves, *Bull. seism. Soc. Am.,* **89**(6), 1535–1542.

Wiechert, E., 1904. Discussion, Verhandlung der zweiten Internationalen Seismologischen Konferenz, *Beitrage Zur Geophys.,* **2,** 41–43.

Yang, Y. & Ritzwoller, M.H., 2008. Characteristics of ambient seismic noise as a source for surface wave tomography, *Geochem. Geophys. Geosyst.,* **9**(2), Q02008, doi:10.1029/2007GC001814.

Yang, Y., Ritzwoller, M.H., Levshin, A.L. & Shapiro, N.M., 2007. Ambient noise Rayleigh wave tomography across Europe, *Geophys. J. Int.,* **168**(1), 259–274.

Yang, Y. *et al.*, 2010. Rayleigh wave phase velocity maps of Tibet and the surrounding regions from ambient seismic noise tomography: Rayleigh wave phase velocities in Tibet, *Geochem. Geophys. Geosyst.,* **11**(8), doi:10.1029/2010GC003119.

Yao, H. & van der Hilst, R.D. 2009. Analysis of ambient noise energy distribution and phase velocity bias in ambient noise tomography, with application to SE Tibet, *Geophys. J. Int.,* **179**(2), 1113–1132.

Yao, H., van Der Hilst, R.D. & De Hoop, M.V., 2006. Surface-wave array tomography in SE Tibet from ambient seismic noise and two-station analysis – I. Phase velocity maps, *Geophys. J. Int.,* **166**(2), 732–744.

Zeng, X. & Ni, S., 2010. A persistent localized microseismic source near the Kyushu Island, Japan: PL microseismic source near Kyushu, *Geophys. Res. Lett.,* **37**(24), doi:10.1029/2010GL045774.

Zhan, Z., Ni, S., Helmberger, D.V. & Clayton, R.W., 2010. Retrieval of Moho-reflected shear wave arrivals from ambient seismic noise, *Geophys. J. Int.,* **182**(1), 408–420.

Zheng, Y., Shen, W., Zhou, L., Yang, Y., Xie, Z. & Ritzwoller, M.H., 2011. Crust and uppermost mantle beneath the North China Craton, northeastern China, and the Sea of Japan from ambient noise tomography, *J. geophys. Res.,* **116,** B12312, doi:10.1029/2011JB008637.